

HIGH RESOLUTION EXPERIMENTS OF VELOCITY AND CONCENTRATION FLUCTUATIONS IN A JET FLOW

Victor Petrov, Thien Duy Nguyen, Daniel Nunez, Akshay Dave and Annalisa Manera

Department of Nuclear Engineering and Radiological Sciences, University of Michigan,

2355 Bonisteel Boulevard, Ann Arbor, MI 48109-2104, USA

petrov@umich.edu; thienn@umich.edu; danielnu@umich.edu; akshayjd@umich.edu

manera@umich.edu

ABSTRACT

In this paper we present a novel experimental technique aimed at the simultaneous measurement of velocity and scalar fluctuations with high spatial and time resolution. Measurements have been performed using wire-mesh sensors in combination with Stereo Particle Image Velocimetry (SPIV) to achieve synchronized measurements of both velocity and scalar fluctuations, and therefore of the turbulent fluxes $u_j'\varphi'$. The proof-of-concept of this measurement technique was obtained on a jet flow experimental facility HiRJet (High Resolution Jet) developed and built in ECMF laboratory at the University of Michigan. Acquired experimental data indicates a high temporal resolution of proposed technique and capabilities of achieving a high level of synchronization which is confirmed by cross-correlation between wire-mesh and SPIV signals.

KEYWORDS

PIV, wire-mesh sensor, CFD, turbulent fluctuations

1. INTRODUCTION

The CFD models most widely used for nuclear safety relevant applications are based on RANS approaches. Though extensive use of higher-fidelity computational techniques such as Large Eddy Simulations (LES) is generally precluded for design and analysis because of the higher computational requirements, this type of simulations is important as a complement to experimental data in order to gain a deeper physical insight in the physical processes under investigation. Therefore, while the validation of LES models is important for gaining more insight in the physics of mixing in presence of buoyant jets and stratified flow conditions, the validation and further development of RANS models is crucial in order to have computational tools suitable for design and safety analyses of nuclear power plants.

The RANS equations are given below, where U represents the mean velocity field, u' the corresponding velocity fluctuations, Φ the mean scalar (e.g. temperature) field and φ' its fluctuation.

$$\frac{\partial \rho}{\partial t} + \frac{\partial(\rho U_j)}{\partial x_j} = 0 \quad (1)$$

$$\frac{\partial(\rho U_i)}{\partial t} + \frac{\partial}{\partial x_j}(\rho U_i U_j) = -\frac{\partial P}{\partial x_i} + \frac{\partial}{\partial x_j} \tau_{ij} - \frac{\partial}{\partial x_j}(\rho \overline{u_i' u_j'}) + g_i(\rho - \rho_0) \quad (2)$$

$$\frac{\partial(\rho \Phi)}{\partial t} + \frac{\partial}{\partial x_j}(\rho \Phi U_j) = \frac{\partial}{\partial x_j} \left(\Gamma \frac{\partial \Phi}{\partial x_j} \right) - \frac{\partial}{\partial x_j}(\rho \overline{u_i' \varphi'}) \quad (3)$$

Closure relationships are needed for the Reynolds stresses $\overline{u_i' u_j'}$ and for turbulent fluxes $\overline{u_j' \varphi'}$. While several modelling formulations exist for the Reynolds stresses, ranging from k-epsilon to more sophisticated Reynolds stress models, accompanied by an extensive experimental database, the modeling

of turbulent fluxes is so far based on the simplistic gradient diffusion hypothesis (SGDH). In this case the unknown correlation between velocity and scalar fluctuation $\overline{u_j' \phi'}$ is modeled to be proportional to the gradient of the mean flow scalar distribution as follow:

$$-\overline{\rho u_j' \phi'} = \frac{\mu_t}{\sigma_t} \frac{\partial \Phi}{\partial x_j} \quad (4)$$

where μ_t is the turbulent viscosity and σ_t is the turbulent Prandtl number. This crude approximation is known to break down in case of buoyancy driven flows, where the effect of density differences on turbulence dominate momentum effects. As a matter of fact, results reported in the literature have shown that the turbulence models currently implemented in CFD commercial codes which are widely employed for the analyses of nuclear components (e.g. ANSYS-CFX, STAR-CCM+, FLUENT) have a tendency to overestimate thermal stratification and underestimate turbulent mixing when buoyancy effects become dominant with respect to momentum effects. This is an indication that the effect of buoyancy on the production and dissipation of turbulent kinetic energy is not correctly modeled (Petrov et al., 2011[1]; Farkas et al., 2010[2]; Scheuerer et al., 2012[3]; Brescianini et al., 2003[4]. For these cases, a more accurate representation of the scalar fluxes $\overline{u_j' \phi'}$ is needed. Modeling becomes even more complicated if stratification is present as well, as it has been observed that in stratified environments the small scales of the passive scalar advected by a turbulent velocity field displays a persisting anisotropy (Bos, 2014[5]). Therefore, the assumption of local isotropy, currently at the basis of most LES subgrid scale (SGS) models, break down in the proximity of the stratified layer. As a matter of fact, SGS models for LES have been developed primarily in the engineering community for homogeneous fluid flows and the applicability of such models to stratified flows have not been investigated exhaustively (Ozgoekmen, 2007[6]).

More sophisticated models aimed at achieving a better representation of the passive scalar fluctuations exist in the literature both for RANS approaches (Worthy, et. Al., 2001[7]) and LES (Basu et al., 2005[8]). However, the experimental database used as basis for the development of those models generally lacks the measurements of the detailed turbulent fluctuations field. In recently published experiments (Duo Xu et al., 2012[9] and Crimaldi JP et al., 2001 [10]) authors combined velocity and scalar field i.e. density measurements for stratified flows. However, experimental technique of simultaneous measurement of velocity and scalar fluctuation at higher temporal resolution and larger measurement area reported in this paper, will help to estimate the turbulent kinetic energy production and dissipation rates due to buoyancy.

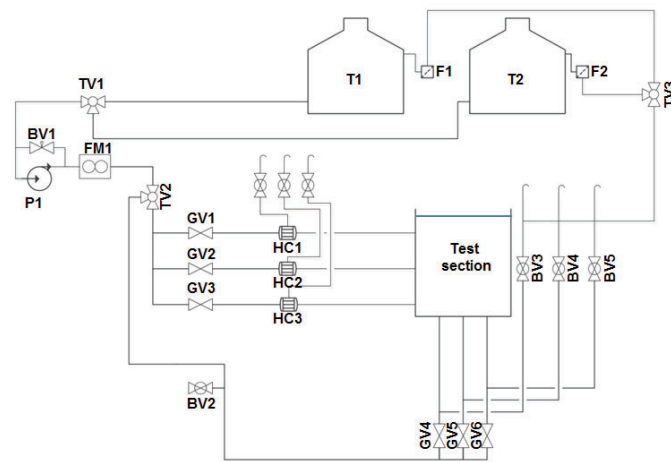
2. EXPERIMENTAL SETUP

2.1. The HiRJet Test Facility

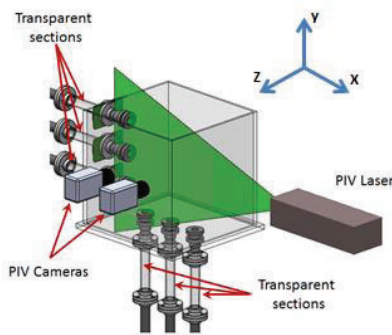
An experimental facility, HiRJet (High Resolution Jet) has been built in the Experimental and Computational Multiphase Flow (ECMF) Laboratory at the University of Michigan. The HiRJet facility is aimed at providing high fidelity time resolved CFD-grade experimental data on concentration/density and velocity fluctuations in momentum and buoyancy driven jet inflows into a relatively large water volume with very well controlled boundary conditions. HiRJet consists of a rectangular water tank having a cross section of 0.61m x 0.585m, and a height of 0.5 m. Six nozzles of 0.038 m ID each are located on the left and bottom walls middle sections and can be used either as flow inlets or outlets. The side nozzles are centered at a distance of 0.152m 0.304m and 0.456m respectively from the bottom of the tank. The central nozzle at the tank bottom is located right in center of the tank, while the left and right bottom nozzles are shifted of 0.165m from the tank center.

Each of the six nozzles is preceded by a 1.8m long straight flow development/stabilization pipe section with an upstream honeycomb flow straightener. All six straight flow sections feature a ~0.3m long optically clear region right before the tank, to allow for a detailed measurement of the inlet velocity profiles by means of Laser Doppler Velocimetry (LDV).

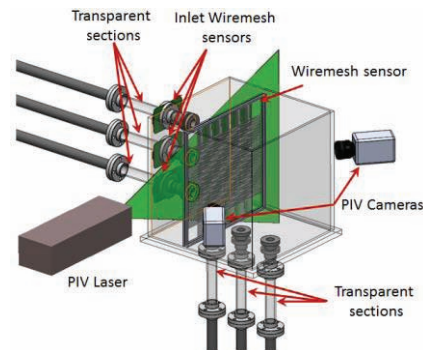
A wide range of inlet flow-rates (0-3kg/s) allows to investigate different operation regimes, from momentum to buoyancy driven flows. The dimensions of the mixing tank have been optimized based on pre-test CFD simulations, so that the effect of the tank walls on the mixing volume of interest is minimized, and a sufficiently large mixing domain with a free-surface is guaranteed. The sections with the flow straighteners are equipped with 3 mm side lines for deaeration. The water level in the mixing tank is adjustable over a range of 0 to 600 mm. Two 400 liters water tanks are used as a source for the tank volume and injection respectively. This configuration allows for experiments using fluids characterized by two different scalar concentrations, or densities. Density variations can be achieved using alcohol, sugar or salt. A scheme of the HiRJet experimental facility, including instrumentation, is reported in figure 1.



(a) Facility scheme



(b) 2D2C PIV experimental setup



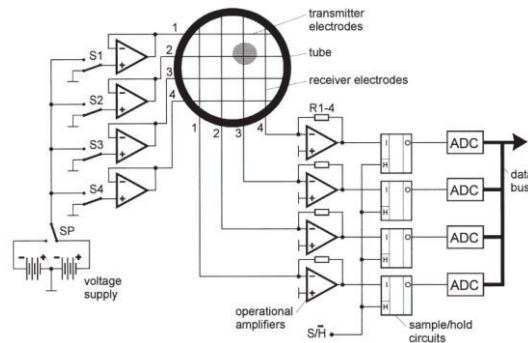
(c) 2D3C PIV experimental setup

Figure 1. Scheme of the HiRJet facility and instrumentation configuration.

HiRJet is equipped with Stereo Particle Image Velocimetry (SPIV) and wire-mesh sensors (WMS). The two measurement systems operate in synchronized mode.

2.2. Wire-mesh Sensor

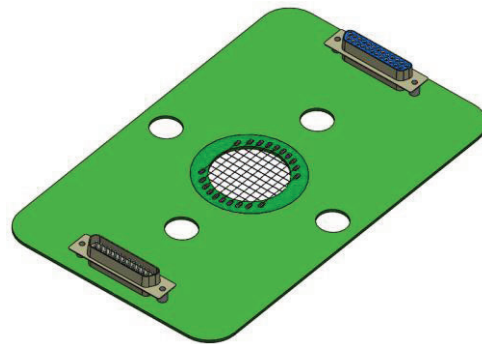
Wire-mesh sensors are used to measure the scalar concentration/density distribution in selected cross-sections of the HiRJet facility, with high spatial (up to 2 mm) and time (up to 10,000 images/s) resolution. Details on the working principle of the sensors are given by Prasser et al. (1998) [11]. A simplified scheme of the sensor is shown in Figure 2 (a). Two wire-mesh sensors are used for the HiRJet facility. One sensor is mounted at the exit of the inlet pipe, upstream of the water tank (see figure 2.c for details). A second sensor, shown in Figure 2.b, is used for the measurement in a cross-section of the water tank. Since the wire-mesh sensors are based on the fluid conductivity, tap and deionized water have been used to distinguish between the water initially present in the tank and the water of the injection.



(a) Simplified scheme of the electrode-mesh device (Prasser et al., 1998)[11].



(b) Tank wire-mesh sensor.



(c) Inlet wire-mesh sensor.

Figure 2. Wire-mesh sensor.

The tank wire-mesh sensor consists of a 96x96 matrix of transmitter and receiver electrodes, for a total of 9216 measurement locations. The electrodes, made of stainless-steel hardened wires with a diameter of 0.1 mm, are fixed to a stainless steel frame and can be mounted at different distances from the inlet pipe, to investigate the spatial evolution of the jet flow. The electrode wires are arranged such that two different wire spatial resolutions of 3.15 mm and 6.3 mm can be obtained on a matrix of 96x96 or 64x64 measurement locations respectively. The axial distance between the receiver and transmitter plane can be easily adjusted using frame spacers of different thickness. For the current experiment an axial distance of 3.3mm was used. . This distance provides large enough gap for the PIV laser sheet to be placed right between transmitter and receiver wires. The wire-mesh sensor of the inlet pipe contains 10x10 transmitter and receiver electrodes with a pitch of 3.8 mm and an axial distance between the electrode planes of 1.5 mm.

2.3. PIV Experimental Setup

Figure 1 (b,c) shows the PIV experimental setup, arranged in a two-dimensional two-component (2D2C) configuration and a (2D3C) stereoscopic configuration respectively. The flow characteristics in the central streamwise-vertical (xy) plane and at a region near the jet exit, i.e. region 1, and at a region far downstream, i.e., region 2, were investigated using the PIV system. The stereo-PIV system was used to study the in-plane velocity components in the vertical-spanwise (yz) plane at a streamwise location $x/D = 4.81$ from the jet exit plane.

The PIV system consists of a high repetition rate Nd:YLF, double cavity, dual head laser (Photonics Industries) with an articulated light arm, two digital CMOS Phantom M340 cameras, and a high speed controller. Each laser beam is capable of up to 30 mJ/pulse at a wavelength of 527 nm. The laser beams are adjusted by means of optical components to form a 2-mm-thick laser sheet. The high-speed Phantom M340 cameras with a full resolution of 2560 x 1600 pixels, a pixel size of $10 \times 10 \mu\text{m}^2$ and 12-bit depth are used to capture the PIV images, which are instantly stored in a 12GB high-speed internal RAM. The high speed controller (LaVision model 1108075) is used for the synchronization between the laser and the cameras. Hollow glass spheres with a mean diameter of $10 \mu\text{m}$ are used as seeding particles. These are mixed both in the storage tank and within the HiRJet water tank so that tracers are present in both the jet and the tank fluid.

In the 2D2C PIV configuration, images of the fluid region in the xy plane are taken, with x/D ranging from -0.2 to 7.8 for region 1 and from 7.1 to 15.2 for region 2 respectively. For each of the two regions (1 and 2), two cameras are used to simultaneously record the experimental images. The fields of views of two cameras and those of two regions are adjoined to enlarge the measured area. A sequence of 1006 image pairs (2560 x 1600 pixels) in a double-frame mode was recorded during each run with a sampling rate of 25 Hz. The inter-pulse time delays were chosen at 2500 μs for region 1, and at 4000 μs for region 2, yielding maximum particle displacements of 12 pixels. To obtain an adequate flow statistics for each region (1 and 2), a total of 3018 image pairs were recorded combining three flow imaging runs.

In the present study, the stereo-PIV measurements were performed in combination with the wire-mesh sensor measurements to simultaneously obtain the instantaneous velocity vector and the concentration fields in the cross-stream plane of the jet. In the stereo-PIV setup, two cameras viewed the yz plane at oblique angles from the streamwise x direction and on either side of the water tank. The camera bodies were adjusted to satisfy the Scheimpflug condition for focusing in the laser sheet. A calibration of the stereo-PIV measurements was done by using a 3D target to map the measurement plane and the image plane (camera sensor plane). The calibration target has dimensions of 0.204m x 0.204m x 0.0143m (width, height and thickness respectively), and includes two plane alternating in depths (3 mm apart) with white markers (size of 3.2 mm) having a spacing of 15 mm in both horizontal and vertical directions. A sequence of 3842 images (1344 x 1600 pixels) in single-frame mode was taken during each run at a sampling rate of 500 Hz. In the stereo-PIV measurements, the out-of-plane velocity was the streamwise velocity, u , which was the dominant component. The time delay between the first and second exposures, defined by the sampling rate in this case, should be small enough to minimize the out-of-plane particle displacements in the cross-plane stereo-PIV measurements.

Image acquisition and image processing were carried out using the DaVis 8.2 software provided by LaVision GmbH. The experimental images were processed by an advanced image deformation multi-pass multi-grid PIV cross-correlation and 50% window overlap for the 2D2C PIV configuration, and 75% window overlap for the stereo-PIV configuration. For both sets of measurements, the first pass started with an interrogation window of 64 x 64 pixels and the final pass ended with an interrogation of 16 x 16 pixels. Vectors were calculated from the correlation map with a Gaussian peak fit for sub-pixel accuracy. Inside each pass, statistical validations were done to identify and correct erroneous vectors. A median

filter was applied and standard deviations of the neighboring vectors were used to filter spurious vectors. The grid spacing in the 2D2C PIV velocity vectors varied from 1.045 mm to 1.044 mm for regions 1 and 2, i.e. $0.0275D$ and $0.0274D$, while it was 0.564 mm in the stereo-PIV vectors, i.e. $0.0148D$. The percentage of bad vectors for all the PIV and stereo-PIV measurements was estimated as 2% and 5%, respectively. The uncertainties in the velocity calculations were estimated to be less than 3% of the mean jet velocity.

2.4. Simultaneous stereo-PIV and Wire-mesh Sensor Measurements

The stereo-PIV and wire-mesh sensor systems were arranged to operate simultaneously, in order to obtain both the velocity and concentration fields. In these measurements, the wire-mesh sensor frame was oriented perpendicularly to the jet main axis and placed at a streamwise location. The laser light-arm formed the laser sheet between wire-mesh electrodes and illuminated the measurement plane aside the tank while two cameras were positioned on the same side of the laser sheet (see Figure 1.c). In this configuration, one camera captured the flow in a forward direction of the scattered light while another camera imaged the light scattered in a backward direction. However, in our first attempt we encountered difficulties when taking the experimental images whose intensities, detected by both cameras with the same f-number, were different. Generally, the backward scattering camera needed an aperture 10 times larger than that of the forward scattering camera. Consequently, the backward camera recorded strong reflections of the laser sheet arising from the interference of the laser sheet with the wire-mesh sensor frame and sensor wires, yielding contamination of the image cross-correlation during the PIV post-processing. This led the estimated particle displacements, calculated from the corresponding correlation peaks, to be not reliable. Three-component (3C) velocity vectors reconstructed by using two cameras were also affected. To avoid using the 3C velocity vectors biased by the backward scattering camera, we only took the two-component (2C) velocity vectors calculated from the forward scattering camera in comparison with the flow concentration obtained by the wire-mesh sensor. Operations of two systems were synchronized by sending a master signal (start-trigger) from the wire-mesh unit to the PIV high speed controller to start the image acquisition of the stereo-PIV and the signal acquisition of the wire-mesh sensor systems. When only velocity components extracted from the forward scattering camera were used, a spatial alignment of wire-mesh sensor with the PIV measurements was achieved by applying an image transformation. This transformation algorithm is based on PIV calibration images to correct image perspective as it is indicated in figure 3. This way wire-mesh cross points coordinates could be obtained using the same coordinate system as for the PIV.

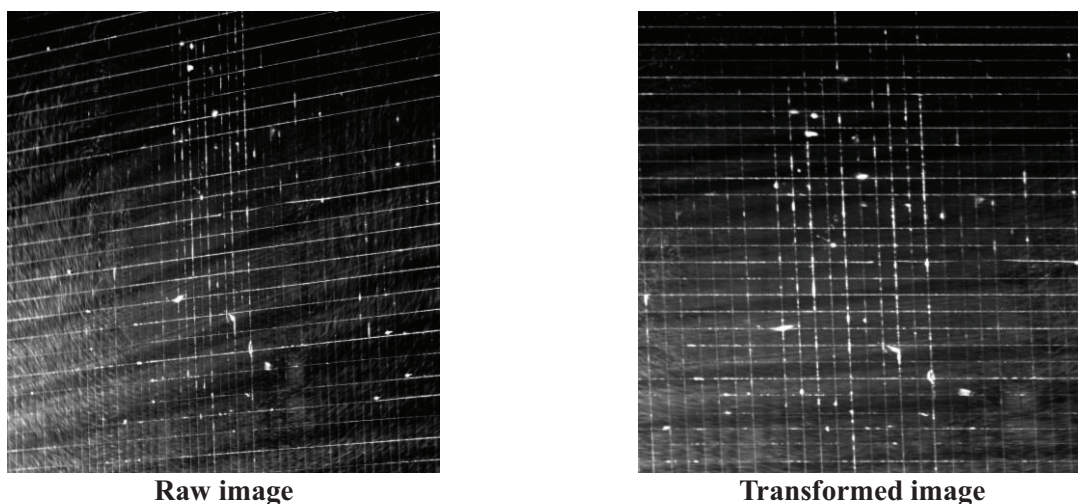


Figure 3. Measurements spatial alignment.

3 EXPERIMENTAL RESULTS

Experiments were performed at a jet Reynolds number $Re_j=5300$, based on the jet exit velocity U_j , the jet diameter D and the kinematic viscosity ν . Water was injected from the HiRJet central side nozzle. The central bottom nozzle was used as outlet instead. All other inlet and outlet nozzles were closed. The x , y and z coordinates, respectively, represent the horizontal, vertical and spanwise directions. The origin of the coordinate system is set at the jet center, in the exit plane of the jet. The velocity components corresponding to the x , y and z directions are U , V and W for the time-averaged velocity and u' , v' and w' for the fluctuating velocity components, respectively.

Two experimental runs were performed where tap water was injected into deionized water in the first run and deionized water was injected into tap water for the second run. The measurement planes were located at 183 mm (4.8D) and 353 mm (9.54D) from the inlet nozzle for first and the second run respectively. Data acquisition started at the time point when injected plug hits the inlet wire-mesh sensor downstream the HiRJet water tank (manual start) For signal analysis 9 points were selected in the jet region for each experimental run, as indicated in figure 4.

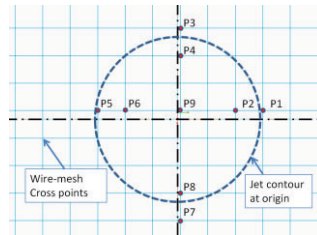


Figure 4. Points for signal processing.

3.1. Standalone Wire-mesh Results.

Wire-mesh data were acquired at a frequency of 500 Hz for total measurement duration of 60 s. Two additional separate runs, of the duration of 1s each, and using only deionized water and only tap water respectively, were performed for calibration purposes.

Concentration fields at the time 1s, 30s and 60s for both runs are reported in figures 5 and 6 respectively, where in left top of each plot the concentration in the inlet nozzle is shown at the same time instant. At a time of 30s the inlet nozzle concentration becomes practically constant and equal to the concentration of the injected fluid. The change of initial concentration in the tank bottom at 60 s is a result of the jet reflection from the wall opposite to the jet inlet. The reflected jet in the second run appears at the top. The reason for this difference could be partly explained by a slight different in density between tap and deionized water (this difference is however less than 1%). The density difference might be also originated from the water heat up caused by the pump. Unfortunately the water temperature was not controlled or measured with any reasonable accuracy at this time.

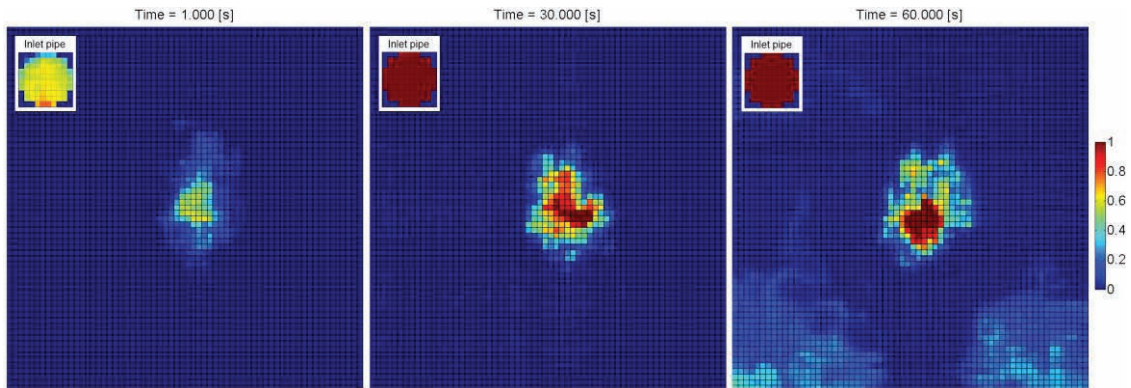


Figure 5. Snapshots of the concentration field in run #1.

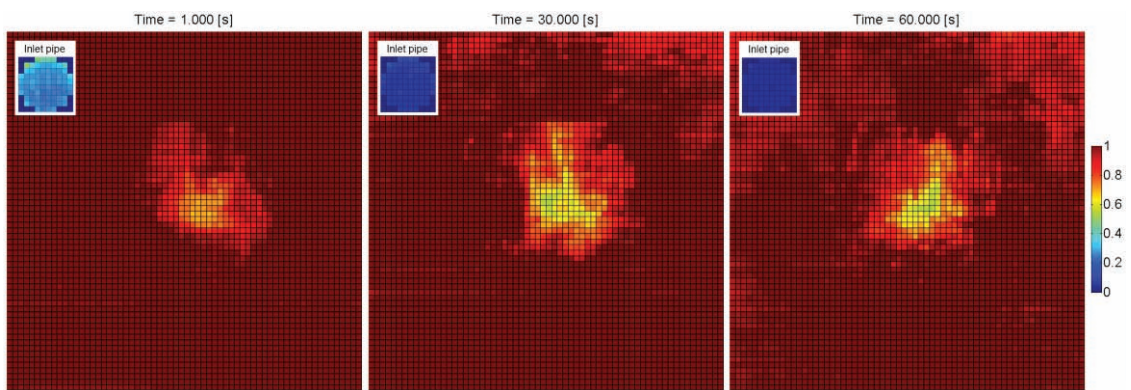


Figure 6. Snapshots of the concentration field in run #2.

The spectrum of the wire-mesh sensors data is shown in figure 7 for both runs. The measured spectra follow the characteristic Kolmogorov's slope of $-5/3$.

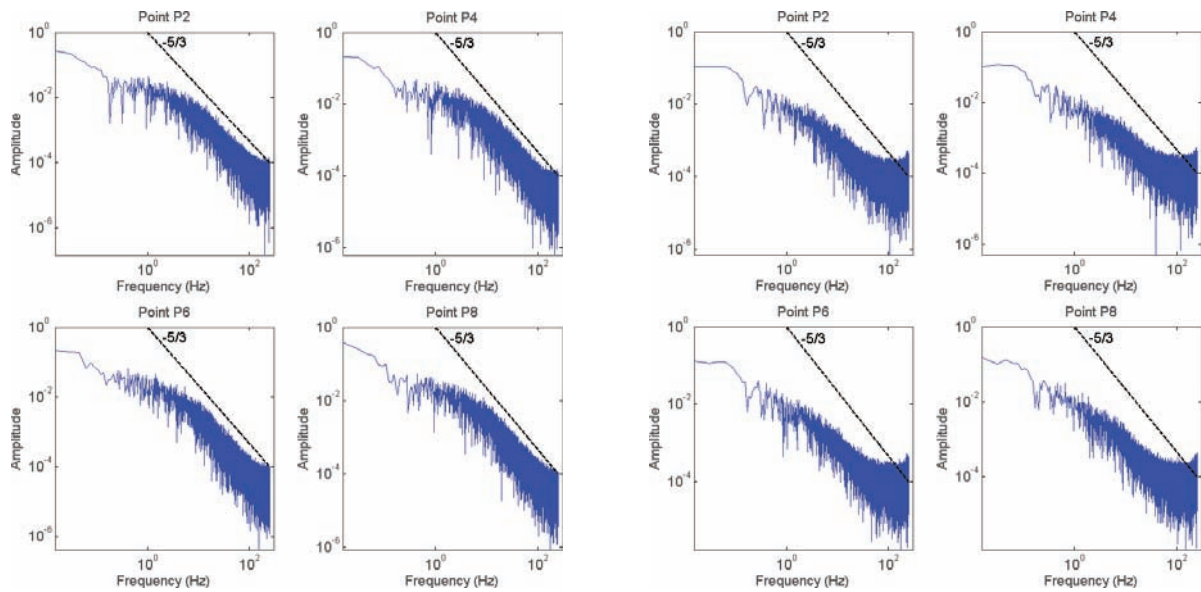


Figure 7. Concentration fluctuation spectra for run 1(left) and run 2(right).

3.2. Standalone PIV Results.

Figure 8 shows the non-dimensionalized mean velocity vectors and turbulent kinetic energy obtained by the PIV measurement. The flow field was merged from the measurements at the region 1 and 2 to yield the full view of the jet development. The jet half-width $y_{1/2}$ is defined as the distance from the vertical point where $U(y_{1/2}) = 0.5U_c$ (U_c is the centerline velocity) towards the centerline. The growth rate of the jet is defined as the ratio of the jet half-width and the jet diameter. In figure 8, the dash lines show the growth rate of the jet from the jet exit to the far end vertical wall of the tank. It is observed that this confinement yielded weak effects to the far field jet velocity by the deflection of the jet growth rate. The potential core length, X_c , was determined by the jet exit to the streamwise location where $U_c(X_c) = 0.95U_j$ and estimated as $3.9D$.

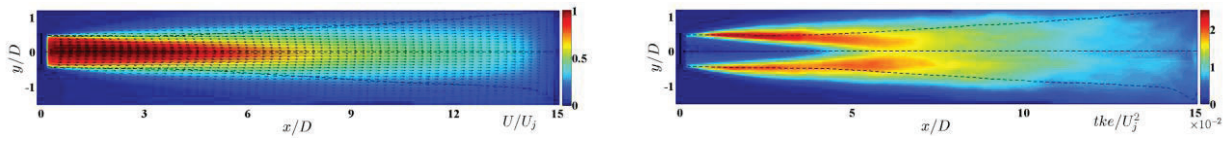


Figure 8: Results obtained from the 2D2C PIV experiments. Non-dimensionalized mean velocity vector field (top), and non-dimensionalized turbulent kinetic energy. Colors shows the magnitude normalized by U_j and U_j^2 , respectively. Dash lines are the growth rate of the jet, defined as $Y_{1/2}/D$, where $Y_{1/2}$ is the jet half-width.

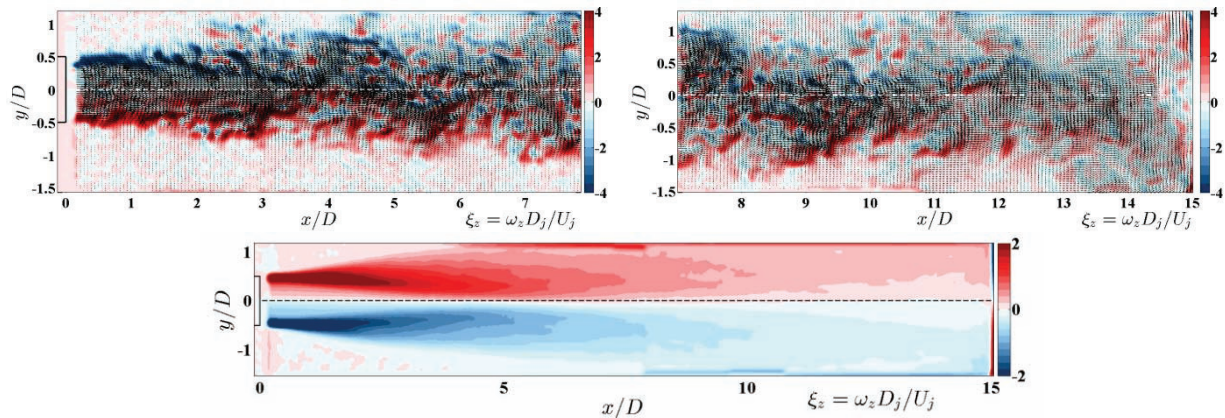


Figure 9: Instantaneous velocity vector and vorticity fields at the region 1 (top-left), region 2 (top-right) and mean vorticity field (bottom) obtained from the 2D2C PIV measurements. The color shows the normalized vorticity magnitude, $\xi_z = \omega_z D / U_j$.

Figure 9 shows two instantaneous velocity vector fields and corresponding vorticity contours at the region 1 (left), region 2 (right) and the mean vorticity (bottom) calculated from the PIV measurements. These plots reveal the generation of the shear layer and vortical structures in the vicinity of the jet. The shear layer originates from the jet exit and rolls into vortices whereas counter-rotating vortices appear on the sides of the jet axis. The shear layers fluctuate in vertical direction and the vortices start to show the flapping motion from the streamwise location of $3 \div 4D$. The rolling vortices travel further downstream and their magnitudes reduce significantly. When the jet flow impinges to the tank end wall, it deflects and diverges on both sides of the jet exit.

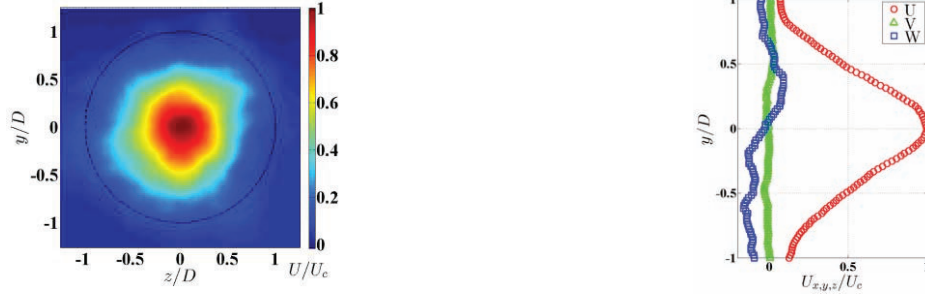


Figure 10: Contour of mean streamwise velocity, U, and profiles of three velocity components, U, V and W obtained by stereo-PIV measurements at streamwise location $X/D = 4.8$.

In figure 10, contour of the mean streamwise velocity, U, obtained from the stereo-PIV measurement at the streamwise location $X/D = 4.8$ is illustrated. This flow measurement was done before placing the wire-mesh sensor to the corresponding location.

In this paragraph, the velocity reconstruction in stereo-PIV measurements is briefly noted. Details on the stereo-PIV experiments can be reviewed in Raffel et al. [12].

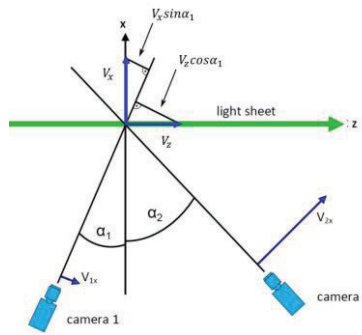


Figure 11: Schematic of stereo-PIV camera arrangement and velocity reconstruction.

Given the arrangement of stereo-PIV cameras in figure 11 (similar to our stereo-PIV experimental setup), V_{1x} and V_{2x} are the measured (projected) velocity components by two stereo-PIV cameras as:

$$V_{1x} = V_z \cos \alpha_1 + V_x \sin \alpha_1 \quad (5)$$

$$V_{2x} = V_z \cos \alpha_2 + V_x \sin \alpha_2 \quad (6)$$

$$V_{1y} = V_{2y} = V_y \quad (7)$$

where (V_x, V_y, V_z) are the true physical velocity components. The velocity reconstruction yields:

$$V_x = (V_{1x} \cos \alpha_2 - V_{2x} \cos \alpha_1) / \sin(\alpha_2 - \alpha_1) \quad (8)$$

$$V_y = (V_{1y} + V_{2y}) / 2 \quad (9)$$

$$V_z = (V_{1x} \sin \alpha_2 - V_{2x} \sin \alpha_1) / \sin(\alpha_2 - \alpha_1) \quad (10)$$

The above equations of velocity reconstruction have indicated that the horizontal displacement measured by each camera is the summation of the V_x and V_z projected on the camera sensor plane. Note that in our current stereo-PIV measurements, the jet axis is perpendicular to the laser plane (measurement plane). It is, therefore, expected that the streamwise velocity component is dominant and mainly contribute to the horizontal velocity detected by each camera.

Indeed, in the comparison of three mean velocity profiles, i.e. U, V and W, shown in figure 10, the streamwise velocity component, U, is dominant while the other two components are significantly smaller by an order of magnitude. This observation supported the use of the two-component velocity vectors calculated from the forward scattering camera when the three-component velocity vectors reconstructed by both forward and backward scattering cameras were negatively affected by the presence of the wire-mesh sensor.

For an extra justification of single camera processing technique reliability the cross correlation as well as Fast Furrier Transformation (FFT) were applied to the velocity values obtained using two camera and single camera processing approaches. This way we can make sure that the difference between the fluctuation amplitude and frequencies along with signal form for both techniques are negligible. According to figure 12 (left) most signal frequencies obtained from stereo velocity reconstruction (SPIV) were adequately discerned by the single camera technique. The signal cross correlations reported in figure 12 (right) have almost autocorrelation shape with a zero lag. The cross-correlation between velocities obtained with a single camera $u_1(\mathbf{x}, t)$ and with two cameras $u_2(\mathbf{x}, t)$ is given by:

$$R_{u\phi} = \frac{1}{N} \sum_{i=1}^N \frac{[u_1(\mathbf{x}, t_i) - \overline{u_1(\mathbf{x}, t)}][u_2(\mathbf{x}, t_i) - \overline{u_2(\mathbf{x}, t)}]}{\sqrt{[u_1(\mathbf{x}, t_i) - \overline{u_1(\mathbf{x}, t)}]^2} \sqrt{[u_2(\mathbf{x}, t_i) - \overline{u_2(\mathbf{x}, t)}]^2}} \quad (11)$$

where N is the number of data samples, and $\overline{u_1}$ and $\overline{u_2}$ stand for the time-averaged values of the velocity respectively. Note that temporal values of velocity and concentration were non-dimensionalized by their standard deviations.

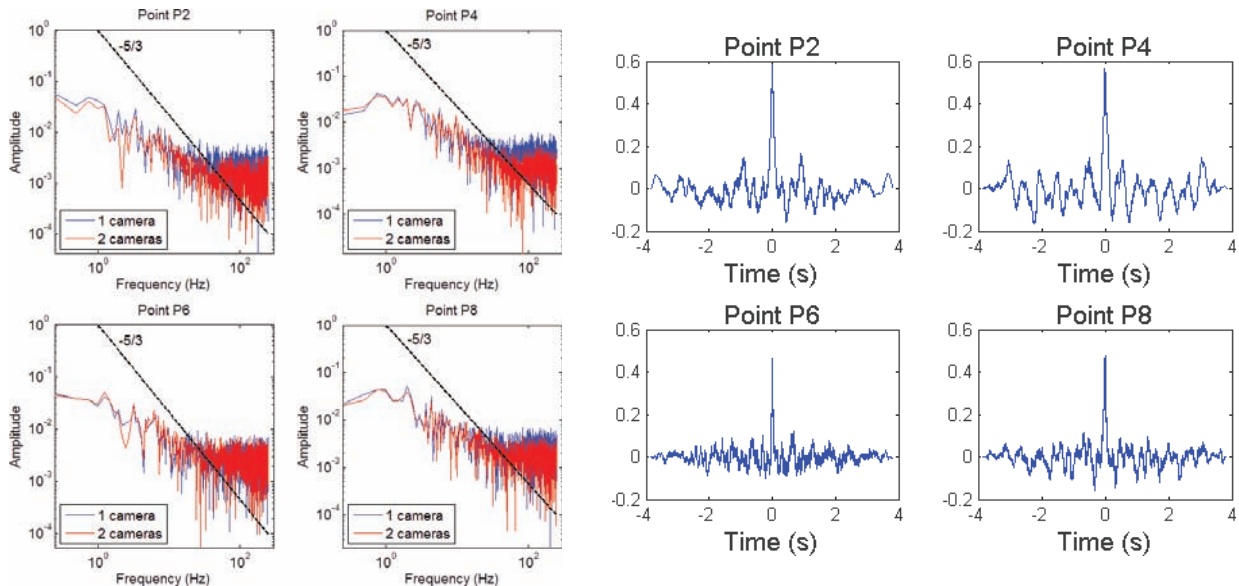


Figure 12. PIV results obtained by velocity reconstruction of 2 cameras vs 1 camera FFT (left) and cross correlation (right).

3.3. Results for Combination Between Wire-mesh and Stereo-PIV.

Comparison of PIV and wire-mesh signals in frequency domain as well as corresponding cross correlations are presented in figures 13 and 14. In this case velocity $u_2(\mathbf{x}, t)$ and its time-averaged value $\overline{u_2}$ in equation (11) were substituted with concentration values obtained by wire-mesh sensor $\Phi(\mathbf{x}, t)$ and $\overline{\Phi}$ respectively. For the first run in the low frequency range most peaks have similar frequencies values with

slightly deviating amplitude caused by the difference in the signal nature and acquisition technique. At higher frequency, the PIV data exhibits higher noise levels. Cross correlation of PIV and concentration signals for the same run in designated points show a strong similarity in the signal form. For the second run cross correlation peaks are not that obvious. Signal coherence deterioration could be explained by even greater image deformation in PIV. Camera position remains the same while measuring plane becomes closer in the second run and this fact leads to increase of α_1 and α_2 angles (see figure 11). At the same time farther distance from the inlet and later timing resulted in extra interface blurring which worked not in favor of strong signal correlation.

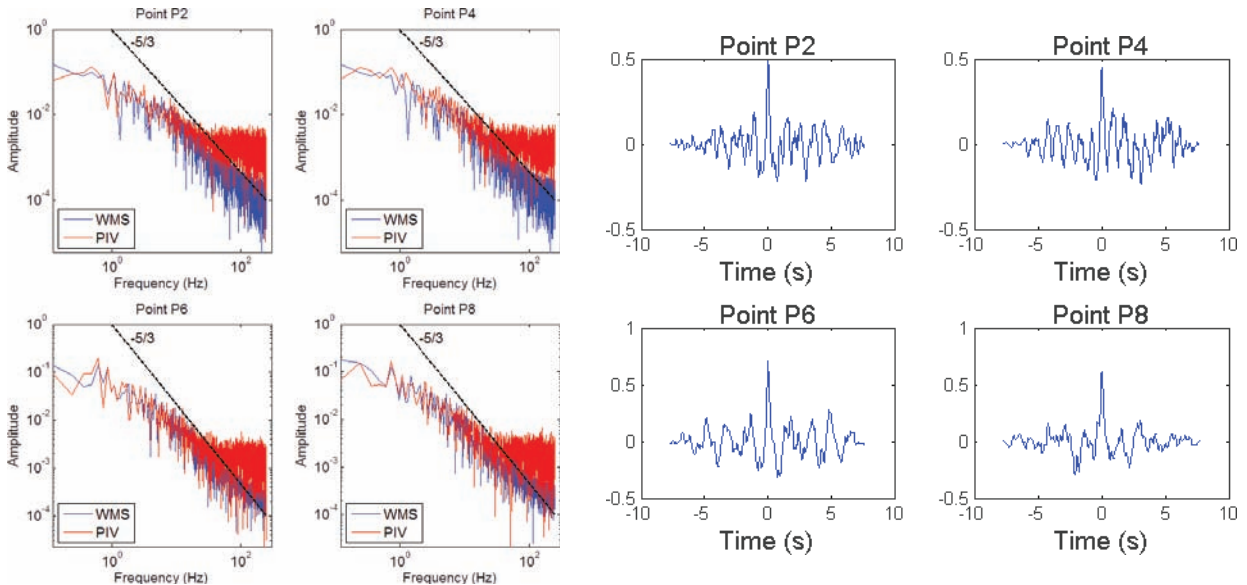


Figure 13. Amplitude spectra (left) and cross correlation (right) of dominant velocity vs. concentration for run #1 calculated for points 2, 4, 6 and 8 (see figure 4)

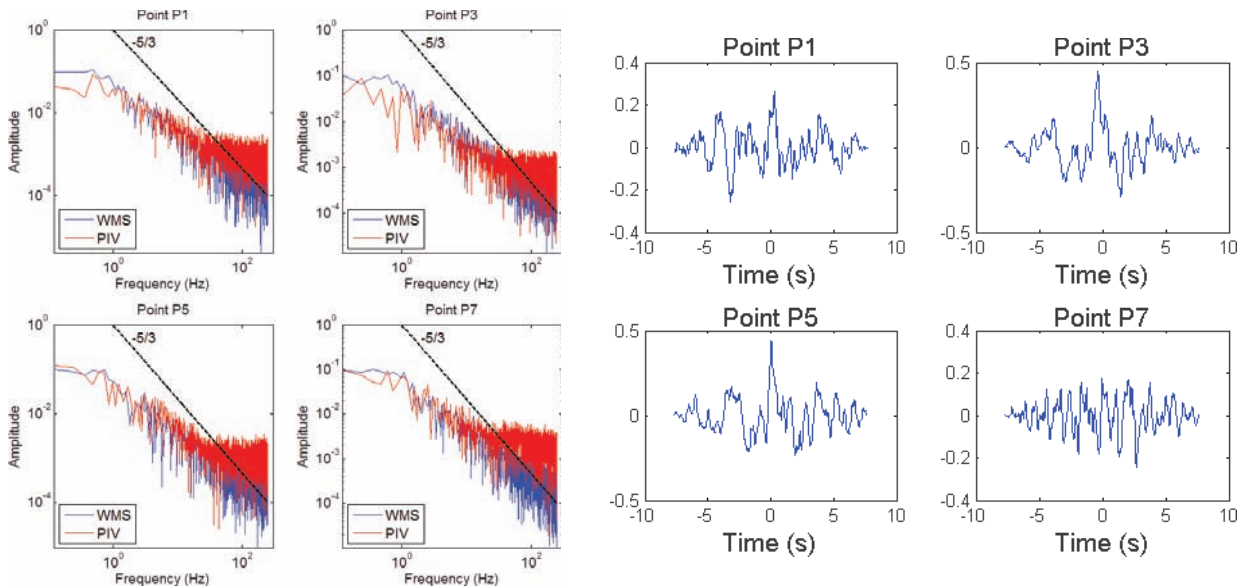


Figure 14. Amplitude spectra (left) and cross correlation (right) of dominant velocity vs. concentration for run #2 calculated for points 1, 3, 5 and 7 (see figure 4).

Spatial correlation performed on the normalized velocity fields obtained with the PIV technique and normalized concentration values for points P2, P4, P6 and P8 are shown in figure 15. Correlations for points P2 and P4 exhibit a quite fuzzy field without strongly dominated picks, even though maximum correlation values are located in a close proximity to the actual point coordinates. Points P6 and P8 correlations present clear correlation peaks instead.

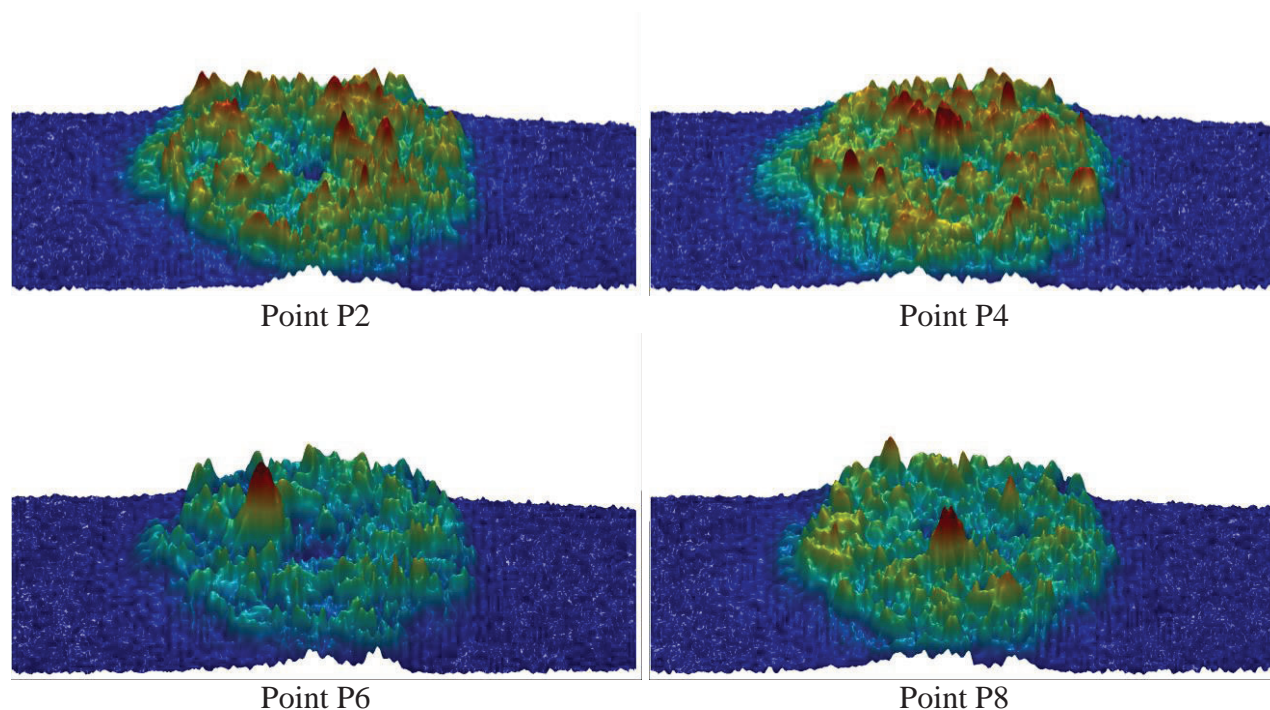


Figure 15. Spatial correlation run #1.

4. CONCLUSIONS

This paper has introduced the combined and synchronized setup of a wire-mesh sensor and a PIV system. This novel development enables the simultaneous measurements of velocity and concentration fields. The results obtained from the experiments have shown an essential signal similarity for both velocity and concentration. The cross-correlation peaks between these signals are considerable and can be promisingly served as the proof-of-concept for the experimental setup and measurement techniques discussed in the paper. During the preliminary tests, difficulties, such as the laser reflection from the stainless steel electrodes and the fluid temperature monitoring, have been encountered and found to yield noises and errors to the recorded signal. In future work, the system will be adapted to mitigate these difficulties, in addition to improving the precise synchronization on data sampling between the PIV and wire-mesh sensor systems at each time frame.

REFERENCES

1. Petrov, V., Manera, A., 2011. Validation of STAR-CCM+ for Buoyancy Driven Mixing in a PWR Reactor Pressure Vessel, *Proc. of 14th Int. Topical Meeting on Nuclear Reactor Thermal-hydraulics (NURETH-14)*, Toronto, Canada, Sept. 25-30.

2. Farkas, T., Toth, I., 2010. FLUENT analysis of a ROSA cold leg stratification test, *Nuclear Engineering and Design*, **240**, 2169 - 2175.
3. Scheuerer, M., Weis, J., 2012. Transient computational fluid dynamic analysis of emergency core cooling injection at natural circulation conditions, *Nuclear Engineering and Design*, **253**, 343–350
4. Brescianini, C.P., Delichatsios, M.A., 2003. New evaluation of the k-epsilon turbulence model for free buoyant plumes, *Numerical Heat Transfer, Part A*, **43**, 731-751.
5. Bos, W.J.T., 2014. On the anisotropy of the turbulent passive scalar in the presence of a mean scalar gradient. *Journal of Fluid Mechanics*, **744**, pp. 38 – 64.
6. Ozgokmena, T. M., Iliescu, T., Fischer, P., Srinivasana, A., Duan, J., 2007. Large eddy simulation of stratified mixing in two-dimensional dam-break problem in a rectangular enclosed domain. *Ocean Modelling*, **16**, pp. 106 – 140.
7. Worthy, J., Sanderson, V., Rubini, P., 2001. Comparison of modified k-epsilon turbulence models for buoyant plumes, *Numerical Heat Transfer, Part B*, **39**, pp. 151 – 165.
8. Basu, S., Porte-Angel, F., 2005. Large-Eddy simulation of stably stratified atmospheric boundary layer turbulence: a scale-dependent dynamic modeling approach. *Journal of the Atmospheric Sciences*, **63**, pp. 2074 – 2091.
9. Duo Xu, Jun Chen. Experimental study of stratified jet by simultaneous measurements of velocity and density fields. *Experiments in Fluids* 2012; **53**: 145.
10. Crimaldi JP, Koseff JR High-resolution measurements of the spatial and temporal scalar structure of a turbulent plume. *Experiments in Fluids* 2001; **31**:90–102
11. H.-M Prasser, A Böttger, J Zschau, A new electrode-mesh tomograph for gas–liquid flows, *Flow Measurement and Instrumentation*, Volume 9, Issue 2, June 1998, Pages 111-119.
12. Raffel M., Willert C., Wereley S., Kompenhans J., Particle image velocimetry: a practical guide. *Springer-Verlag*; 2007.